Characterization of a Reactive Rh_2 Nitrenoid by Crystalline Matrix Isolation

Anuvab Das,[1] Yu-Sheng Chen,[2] Joseph H. Reibenspies,[1] David C. Powers[1,*]

[1]Department of Chemistry, Texas A&M University, College Station, TX 77843, USA
[2]ChemMatCARS, University of Chicago c/o APS/ANL, Argonne, IL 60439, USA
*powers@chem.tamu.edu

Abstract Fleeting lifetimes of reactive intermediates in C–H functionalization chemistry often prevent their direct characterization. For example, the critical nitrenoid intermediates that mediate Rh_2-catalyzed C–H amination have eluded characterization for more than 40 years. In the absence of structural characterization of these species, methodological development is often computationally guided. Here we report the first X-ray crystal structure of a reactive Rh_2 nitrenoid, enabled by N_2 elimination from an organic azide ligand within a single-crystal matrix. The resulting high-resolution data set demonstrates a long Rh–N bond, consistent with a triplet electronic structure. The demonstration of facile access to reactive metal nitrenoids within a crystalline matrix provides a platform for structural characterization of the elusive transient species at the heart of C–H functionalization.

Unstabilized nitrenes are reactive, high-energy species that feature a hextet electronic configuration at nitrogen.[1] Nitrenes participate in a diverse reaction manifold, including C–H insertion, addition to C–C multiple bonds, and various unimolecular rearrangements that render these species challenging to utilize as intermediates in selective synthetic chemistry ([2]). Synthetic chemists[3-9] and biologists[10-12] have advanced selective nitrene-transfer chemistry that is predicated on leveraging the reactivity of transition metal-stabilized nitrenoid intermediates. In particular, Rh_2-catalysis has emerged as a broadly useful platform in nitrene-transfer catalysis (Fig. 1).[13-20]

The critical Rh_2 nitrenoid intermediate proposed to be responsible for C–H amination and olefin aziridination has been detected by mass spectrometry[21] and time-resolved spectroscopic methods,[22] but due to the fleeting lifetime of these species, structural data of these transient species has been unavailable. Critical issues, such as the preferred electronic configuration of Rh_2 nitrenoids, have not been resolved despite extensive theoretical interest.[23-25]

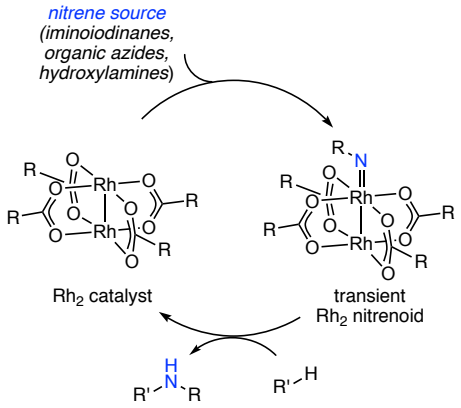

Figure 1. Rh_2-catalyzed nitrene transfer chemistry has emerged as a leading method for introducing nitrogen content in organic molecules. These reactions are proposed to proceed via transient Rh_2 nitrenoids, which have thus far eluded structural characterization.

Unambiguous molecular structure determination can be achieved by X-ray diffraction, but requires chemical samples that are sufficiently kinetically stable to be crystallized. The inherently transient nature of reactive intermediates largely precludes application of X-ray diffraction to the characterization of these species. Two methods have been advanced to gain structural information about reactive intermediates in the condensed phase: 1) structural characterization of synthetic derivatives designed to attenuate the reactivity of the intermediate of interest, for example via introduction of sterically encumbering ligands,[26-29] and 2) spectroscopic characterization of photogenerated reactive intermediates by cryogenic matrix isolation.[30] We envisioned that photogeneration of reactive intermediates within a crystalline matrix would combine classical matrix isolation with X-ray diffraction and enable structural characterization of these species without synthetic derivatization.[31] Here, we demonstrate the successful application of this strategy

to the characterization of a Rh_2 nitrenoid generated by N_2 elimination from a Rh_2 alkylazide complex within a crystalline matrix.

We have pursued characterization of nitrenoid supported by $Rh_2(esp)_2$ (**1**), a complex in which the Rh_2 core is supported by two chelating *bis*-carboxylate ligands.[15] Complex **1** has emerged a particularly effective, and widely utilized, nitrene-transfer catalyst.[15,17-20] We targeted the synthesis of Rh_2 complexes with organic azide ligands based on the hypothesis the facile N_2 extrusion would provide access to Rh_2 nitrenoids. Exposure of $Rh_2(esp)_2$ to CH_2Cl_2 solutions of AdN_3 resulted in sequential formation of two Rh_2 azide adducts: $Rh_2(esp)_2(AdN_3)$ (**2a**) and $Rh_2(esp)_2(AdN_3)_2$ (**2b**). Concentration-dependent UV-vis spectra display isosbestic points connecting $Rh_2(esp)_2$ (**1**) and $Rh_2(esp)_2(AdN_3)$ (**2a**) at 0–12 mM [AdN_3] and isosbestic points connecting **2a** and $Rh_2(esp)_2(AdN_3)_2$ (**2b**) at 12–85 mM [AdN_3] implying the absence of steady-state intermediates in these reactions (Fig. S1). Further spectral evolution was not observed upon further addition of AdN_3. Jobs analysis confirms that **2a** is a 1 : 1 adduct of $Rh_2(esp)_2$ and AdN_3 (Fig. S2 and Table S1). Rapid exchange of free and bound AdN_3 is evident in the room temperature ^{1}H NMR spectra of **2a** and **2b**. Low-temperature ^{1}H NMR spectroscopy and electrospray ionization-mass spectrometry (ESI-MS) support the formulation of **2a** and **2b** as *mono*- and *bis*-azide adducts, respectively (Figs. S3 and S4). The AdN_3 ligands are weakly bound; titration of a tetrahydrofuran solution of $Rh_2(esp)_2$ with AdN_3 results in no spectral changes, which suggests preferential binding of THF at the apical sites of $Rh_2(esp)_2$.

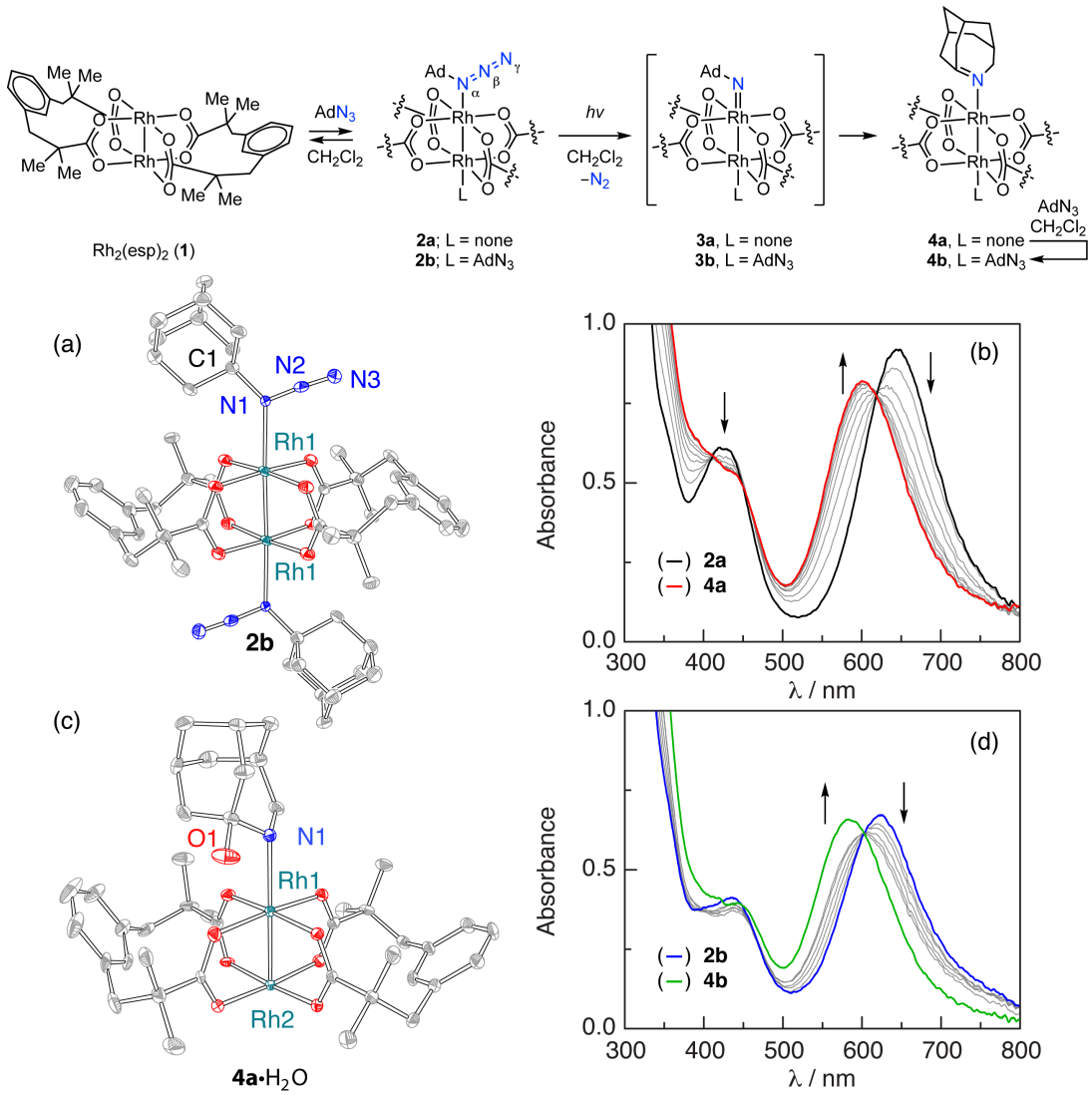

Figure 2. Treatment of $Rh_2(esp)_2$ (**1**) with AdN_3 results in sequential formation of $Rh_2(esp)_2(AdN_3)$ (**2a**) and $Rh_2(esp)_2(AdN_3)_2$ (**2b**). (a) Thermal ellipsoid plot of **2b** drawn at 50% probability with H-atoms and solvent removed for clarity; Rh(1)–Rh(1): 2.3968(8) Å, Rh(1)–N(1): 2.335(3) Å, N(1)–C(1): 1.509(5) Å, N(1)–N(2): 1.254(5) Å, N(2)–N(3): 1.135(5) Å, N(1)–N(2)–N(3): 176.1(4)°. (b) UV-vis spectra collected during the photolysis of Rh_2 complex **2a** in CH_2Cl_2 (335 nm < λ < 610 nm). Isosbestic points are observed at 411, 455, and 618 nm, which indicate the lack of a steady-state intermediate in the conversion of **2a** to **4a**. (c) Thermal ellipsoid plot of **4a**·H_2O drawn at 50% probability with H-atoms and solvent removed for clarity. Selected metrical parameters: Rh(1)–Rh(2): 2.3959(5) Å; Rh(1)–N(1): 2.303(4) Å. (d) UV-vis spectra collected during the photolysis of Rh_2 complex **2b** in CH_2Cl_2 (335 nm < λ < 610 nm). An isosbestic point is observed at 603 nm, which indicates the lack of a steady-state intermediate in the conversion of **2b** to **4b**.

Single crystals of **2b** were obtained from cooling a CH_2Cl_2 solution of $Rh_2(esp)_2$ and AdN_3. X-ray diffraction analysis revealed the structure depicted in Figure 2a in which two symmetry-equivalent AdN_3 ligands are bound to the Rh_2 core via N(α). Efforts to crystallize **2a** by lowering

the AdN_3 loading consistently provided *bis*-azide adduct **2b** as the exclusive crystallization product, which suggests the preferential crystallization of **2b** over *mono*-azide adduct **2a**. The Rh–Rh distance in **2b** is 2.3968(8) Å, which is similar to that previously reported for $Rh_2(esp)_2S_2$ complexes (see Table S2). The N_3 fragment of the AdN_3 ligand is nearly linear (N(1)–N(2)–N(3) = 176.2(4)°), the N(1)–N(2) and N(2)–N(3) distances are similar to those in free AdN_3, and the infrared (IR) spectrum of **2b** displays υ_{N3} at 2120 and 2093 cm^{-1} (Fig. S5). These metrics are consistent with AdN_3 binding as a σ-donor with insignificant π-backbonding.[32]

Rh_2 complexes **2a** and **2b** are photoprecursors to Rh_2 nitrenoids. Photolysis of a CH_2Cl_2 solution of **2a** (335 nm < λ < 610 nm) resulted in new spectral features that are accessed via well-anchored isosbestic points at 411, 455, and 618 nm (Fig. 2b). Crystallization of the photolysis reaction mixture afforded a single crystal of **4a**·H_2O (Fig. 2c). Compound **4a**·H_2O can be envisioned as arising from nitrogen-atom insertion into the C–C bond of the adamantyl group to generate a transient 2-azahomoadamant-3-ene ligand, which is trapped with water to give rise to the observed hemiaminal ligand. The observed structure is consistent both with the known low-temperature rearrangement of adamantyl nitrene and with the electrophilicity of highly strained anti-Bredt imines.[33] The UV-vis spectrum of a CH_2Cl_2 solution of **4a**·H_2O is well-matched to the UV-vis spectrum obtained following photolysis of **2a** (Fig. S6). Similarly, photolysis of complex **2b** (335 nm < λ < 610 nm) proceeds via a well-anchored isosbestic point at 603 nm (Fig. 2d). The product of photolysis was assigned as **4b** by comparison of the final UV-vis spectrum obtained from photolysis of **2b** with the spectrum generated by addition of AdN_3 to **4a**·H_2O (Fig. S7).

Matrix-assisted laser desorption-mass spectrometry (MALDI-MS) data provided additional evidence for the facile elimination of N_2 from **2** (Fig. 3). Ablation of a sample of **2a** produces an ion at *m/z* = 907.5, which is well matched to the expected mass of $Rh_2(esp)_2(AdN)^+$ (calc = 907.2),

and is well matched to the expected isotopic distribution. Ablation of a sample of [^{15}N]-**2a**, prepared from monolabeled [^{15}N]-AdN$_3$, provided the expected +1 m/z (*m/z* = 908.4 (expt); 908.2 (calc)). The isotope pattern is well-matched to a 1:1 mixture of **2a** and [^{15}N]-**2a** that is expected based on incorporation of 50% ^{15}N at each of N(α) and N(γ). *In situ* IR analysis of both photolyzed or thermolyzed KBr pellets of **2b** further indicate facile N$_2$ loss from **2b** (Figs. S8 and S9).

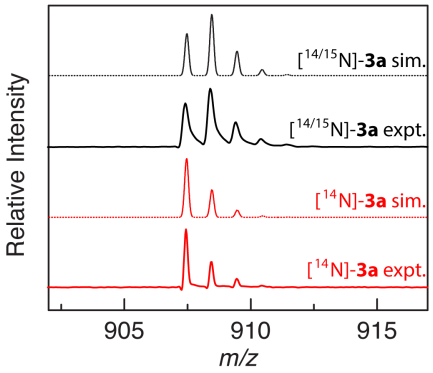

Figure 3. MALDI-MS data acquired for ablation of samples of **2a** and [^{15}N]-**2a**, which indicate the facile loss of N$_2$ from these complexes to generate Rh$_2$(esp)$_2$(AdN) fragments.

We hypothesized that low-temperature N$_2$ extrusion from **2b** within a single crystal habit would enable direct structural characterization of nitrenoid **3b**. To this end, we examined the *in situ* structural evolution of a single-crystal of **2b** by X-ray diffraction during irradiation with a 365 nm light source. Data was collected at 100 K with 50 keV synchrotron radiation.[34] Solid-state reaction progress was monitored by free refinement of the nitrogen occupancies, which indicate that while the occupancy of N(α) was unchanged with time, the occupancy of N(β) decreased. Concurrently, the space group was observed to transition from monoclinic P2$_1$/c to P2$_1$/n. Refinement of the resulting data indicated elimination of a molecule of N$_2$ to afford Rh$_2$ nitrenoid **3b**·N$_2$ (Fig. 4). Upon N$_2$ extrusion, Rh(1)–N(1B) (*i.e.* the nitrenoid linkage) contracts from 2.335(3) Å (**2b**) to 2.12(1) Å (**3b**). Concurrent with N$_2$ extrusion and Rh(1)–N(1B) contraction, significant contraction of N(1B)–C(1) (*i.e.* the N–C bond in the adamantyl nitrene fragment) is also observed from 1.509(5) Å (**2b**) to 1.41(2) Å (**3b**). No substantial changes in the C–C distances

of the adamantyl fragment were observed, and both Rh(1)–Rh(1) (2.3968(8) Å (**2b**); 2.3903(4) Å (**3b**)) and Rh(1)–N(1A) (*i.e.* the Rh–N(Ad)N_2 linkage; 2.335(3) (**2b**); 2.346(4) Å (**3b**)) are essentially unchanged. The Rh centers in **3b**·N_2 are symmetry equivalent, and thus following loss of N_2 the AdN_3 and AdN ligands of **3b** are compositionally disordered (*i.e.* 50% occupancy of each AdN and AdN_3 on each of the Rh centers). Solid-state conversion of up to 70% are well accommodated within the single crystal. Attempts to achieve higher conversions or to promote loss of a second equivalent of N_2 to generate a *bis*-nitrenoid by prolonged irradiation were unsuccessful due to loss of crystallinity (see Supporting Information for details).

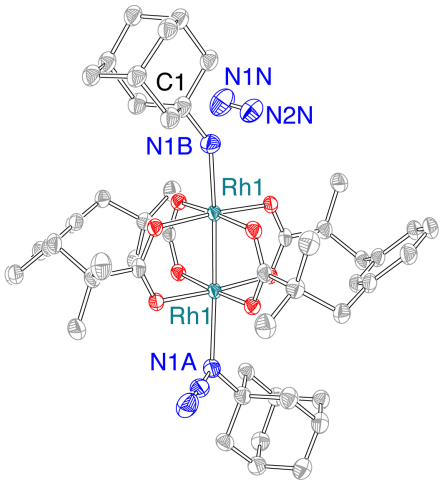

	3b expt.	^{3}[**3b**] comp.	^{1}[**3b**] comp.
Rh(1)–N(1B)	2.12(2)	2.098	1.934
Rh(1)–N(1A)	2.346(4)	2.399	2.605
N(1B)–C(1)	1.41(2)	1.411	1.385
Rh(1)–Rh(1)	2.3903(4)	2.439	2.466

Figure 4. Thermal ellipsoid plot of **3b**·N_2 generated by solid-state N_2 elimination from **2b**. Ellipsoids are drawn at 50% probability. H-atoms and solvent are removed for clarity. The structure illustrated here results from refinement of a data set collected at 46% conversion; higher conversions can be achieved but at the expense of crystallinity (see Supporting Information). Comparison of the bond metrics derived from the X-ray structure with those of ^{3}[**3b**] and ^{1}[**3b**] indicate much closer agreement with the triplet electronic configuration.

Density Functional Theory (DFT) optimization of the geometry of **3b** has been pursued both as a singlet and as a triplet electronic configuration (*i.e.* ^{1}[**3b**] and ^{3}[**3b**]; M06 functional, LANL2DZ basis set for Rh, 6-31G** for other atoms; see Supporting Information for computational details). The calculated Rh(1)–Rh(1), Rh(1)–N(1A), Rh(1)–N(1B), and N(1B)–

C(1) distances for ^{3}[**3b**] are in excellent agreement with the experimentally defined parameters (Fig. 4). In contrast, the optimized structure of ^{1}[**3b**] substantially underestimates the Rh(1)–N(1B) distance (1.934 Å (comp.); 2.12(2) Å (expt.)) and substantially overestimates the Rh(1)–N(1A) distance (2.605 Å (comp.); 2.346(4) Å (expt.)). The observation of ^{3}[**3b**] is consistent with the relative stabilities computed for the ^{1}[**3b**] and ^{3}[**3b**]; the singlet structure is calculated to be 16.8 kcal/mol above the triplet. We have also examined the impact of the apical ligand on the computed metrics for ^{3}[Rh_2=NAd] complexes by either removing the distal AdN_3 ligand of **3b** or replacing it with amine, imine, or nitrene ligands. These calculations reveal that the Rh=NAd distance is highly sensitive to the identity of the apical ligand on the distal Rh center (*i.e.* 2.022 Å with no ligand; 2.153 Å with an *t*-$BuNH_2$) and that the best agreement between theory and experiment arises from an AdN_3 ligand on the distal Rh center.

Typically, structural characterization of the transient intermediates involved in the intimate bond-forming and -breaking processes during catalysis is not possible. Investigations of reaction mechanisms often rely on computational characterization of reactive intermediates using methods optimized for isolated catalyst intermediates. The characterization of nitrenoid **3b** reported here establishes the electronic and three-dimensional structures of this critical intermediate, and as such, provides insights that we anticipate will inform ongoing development of C–H amination chemistry. The demonstration of crystalline matrix confinement as a platform for the structural characterization of reactive intermediates raises the tantalizing possibility that proper design of photoactive molecular precursors may represent a general strategy to directly characterize reactive species generated by elimination of small molecules within crystalline samples.

References

(1) Wentrup, C. Carbenes and Nitrenes: Recent Developments in Fundamental Chemistry. *Angew. Chem. Int. Ed.* **57**, 11508–11521 (2018).

(2) Dequirez, G.; Pons, V.; Dauben, P. Nitrene Chemistry in Organic Synthesis: Still in Its Infancy? *Angew. Chem. Int. Ed.* **51**, 7384–7395 (2012).

(3) Davies, H. M. L.; Manning, J. R. Catalytic C–H Functionalization by Metal Carbenoid and Nitrenoid Insertion. *Nature* **451**, 417–424 (2008).

(4) Roizen, J. L.; Harvey, M. E.; Du Bois, J. Metal-Catalyzed Nitrogen-Atom Transfer Methods for the Oxidation of Aliphatic C–H Bonds. *Acc. Chem. Res.* **45**, 911–922 (2012).

(5) Gephart, R. T., III; Warren, T. H. Copper-Catalyzed sp^3 C–H Amination. *Organometallics* **31**, 7728–7752 (2012).

(6) Alderson, J. M.; Corbin, J. R.; Schomaker, J. M. Tunable, Chemo- and Site-Selective Nitrene Transfer Reactions through the Rational Design of Silver(I) Catalysts. *Acc. Chem. Res.* **50**, 2147–2158 (2017).

(7) Park, Y.; Kim, Y.; Chang, S. Transition Metal-Catalyzed C–H Amination: Scope, Mechanism, and Applications. *Chem. Rev.* **117**, 9247–9301 (2017).

(8) Singh, R.; Mukherjee, A. Metalloporphyrin Catalyzed C–H Amination. *ACS Catal.* **9**, 3604–3617 (2019).

(9) Svastits, E. W.; Dawson, J. H.; Breslow, R.; Gellman, S. H. Functionalized Nitrogen Atom Transfer Catalyzed by Cytochrome P-450. *J. Am. Chem. Soc.* **107**, 6427–6428 (1985).

(10) Brandenberg, O. F.; Fasan, R.; Arnold, F. H. Exploiting and engineering hemoproteins for abiological carbene and nitrene transfer reactions. *Curr. Opin. Biotechnol.* **47**, 102–111 (2017).

(11) Prier, C.; Zhang, R. K.; Buller, A. R.; Brinkmann-Chen, S.; Arnold, F. H. Enantioselective, intermolecular benzylic C–H amination catalyzed by an engineered iron-haem enzyme. *Nat. Chem.* **9**, 629–634 (2017).

(12) Cho, I.; Jia, Z.-J.; Arnold, F. H. Genetically Tunable Enzymatic C–H Amidation for Lactam Synthesis. *Science* **364**, 575–578 (2019).

(13) Nägeli, I.; Baud, C.; Bernardinelli, G.; Jacquier, Y.; Moran, M.; Müller. P. Rhodium(II)-Catalyzed CH Insertions with {[(4-Nitrophenyl)sulfonyl]imino}phenyl-λ^3-iodane. *Helv. Chim. Acta* **80**, 1087–1105 (1997).

(14) Espino, C. G.; Wehn, P. M.; Chow, J.; Du Bois, J. Synthesis of 1,3–Difunctionalized Amine Derivatives through Selective C–H Bond Oxidation. *J. Am. Chem. Soc.* **123**, 6935–6936 (2001).

(15) Espino, C. G.; Fiori, K. W.; Kim, M.; Du Bois, J. Expanding the Scope of C–H Amination through Catalyst Design. *J. Am. Chem. Soc.* **126**, 15378–15379 (2004).

(16) Stokes, B. J.; Dong, H.; Leslie, B. E.; Pumphrey, A. L.; Driver, T. G. Intramolecular C–H Amination Reactions: Exploitation of the Rh_2(II)-Catalyzed Decomposition of Azidoacrylates. *J. Am. Chem. Soc.* **129**, 7500–7501 (2007).

(17) Nguyen, Q.; Sun, K.; Driver, T. G. Rh_2(II)-Catalyzed Intramolecular Aliphatic C–H Bond Amination Reactions using Aryl Azides as the *N*-Atom Source. *J. Am. Chem. Soc.* **134**, 7262–7265 (2012).

(18) Jat, J. L.; Paudyal, M. P.; Gao, H.; Xu, Q.-L.; Yousufuddin, M.; Devarajan, D.; Ess, D. H.; Kürti, L.; Falck, J.R. Direct and Stereospecific Synthesis of Unprotected N-H and N-Me Aziridines from Olefins. *Science* **343**, 61–65 (2014).

(19) Paudyal, M. P.; Adebesin, A. M.; Burt, S. R.; Ess, D. H.; Ma, Z.; Kürti, L.; Falck, J. R. Dirhodium-catalyzed C-H arene amination using hydroxylamines. *Science* **353**, 1144–1147 (2016).

(20) Chiappini, N. D.; Mack, J. B. C.; Du Bois, J. Intermolecular C(sp^3)–H Amination of Complex Molecules. *Angew. Chem. Int. Ed.* **57**, 4956–4959 (2018).

(21) Perry, R. H.; Cahill, T. J., III; Roizen, J. L.; Du Bois, J.; Zare, R. N. Capturing fleeting intermediates in a catalytic C–H amination reaction cycle. *Proc. Nat. Acad. Sci. USA* **109**, 18295–18299 (2012).

(22) Das, A.; Maher, A. G.; Telser, J.; Powers, D. C. Observation of a Photogenerated Rh_2 Nitrenoid Intermediate in C–H Amination. *J. Am. Chem. Soc.* **140**, 10412–10415 (2018).

(23) Varela-Álvarez, A.; Yang, T.; Jennings, H.; Kornecki, K. P.; Macmillan, S. N.; Lancaster, K. M.; Mack, J. B. C.; Du Bois, J.; Berry, J. F.; Musaev, D. G. Rh_2(II,III) Catalysts with Chelating Carboxylate and Carboxamidate Supports: Electronic Structure and Nitrene Transfer Reactivity. *J. Am. Chem. Soc.* **138**, 2327–2341 (2016).

(24) Wang, J.; Zhao, C.; Weng, Y.; Xu, H. Insight into the mechanism and site-selectivity of $Rh_2^{II,II}(esp)_2$-catalyzed intermolecular C–H amination. *Catal. Sci. Technol.* **6**, 5292–5303 (2016).

(25) Harrison, J. G.; Gutierrez, O.; Jana, N.; Driver, T. G.; Tantillo, D. J. Mechanism of Rh_2(II,II)-Catalyzed Indole Formation: The Catalyst Does Not Control Selectivity. *J. Am. Chem. Soc.* **138**, 487–490 (2016).

(26) For examples in the context of reactive metal nitrenoid fragments, see references 26-29: Bakhoda, A.; Jiang, Q.; Bertke, J. A.; Cundari, T. R.; Warren, T. H. Elusive Terminal Copper Arylnitrene Intermediates. *Angew. Chem. Int. Ed.* **56**, 6426–6430 (2017).
(27) Iovan, D. A.; Betley, T. A. Characterization of Iron-Imido Species Relevant for *N*-Group Transfer Chemistry. *J. Am. Chem. Soc.* **138**, 1983–1993 (2016).
(28) Laskowski, C. A.; Miller, A. J. M.; Hillhouse, G. L.; Cundari, T. R. *J. Am. Chem. Soc.* **2011**, *133*, 771–773.
(29) Shay, D. T.; Yap, G. P. A.; Zakharov, L. N.; Rheingold, A. L.; Theopold, K. H. Intramolecular C–H Activation by an Open-Shell Cobalt(III) Imido Complex. **44**, 1508–1510 (2005).
(30) Downs, A. J.; Greene, T. M. Coming to Grips with Reactive Intermediates. *Adv. Inorg. Chem.* **46**, 101–171 (1999).
(31) Das, A.; Reibenspies, J. H.; Chen, Y.-S.; Powers, D. C. Direct Characterization of a Reactive Lattice-Confined Ru_2 Nitride by Photocrystallography. *J. Am. Chem. Soc.* **139**, 2912–2915 (2017).
(32) Dias, H. V. R.; Polach, S. A.; Goh, S.-K.; Archibong, E. F.; Marynick, D. S. Copper and silver complexes containing organic azide ligands: syntheses, structures, and theoretical investigation of $[HB(3,5\text{-}(CF_3)_2Pz)_3]CuNNN(1\text{-Ad})$ and $[HB(3,5\text{-}(CF_3)_2Pz)_3]AgN(1\text{-Ad})NN$ (where Pz = Pyrazolyl and 1-Ad = 1-Adamantyl). *Inorg. Chem.* **39**, 3894–3901 (2000).
(33) Dunkin, I. R.; Shields, C. J.; Quast, H.; Seiferling, B. The Photolysis of 1-Azido-4-Methylbicyclo[2.2.2]octane and 1-Azidoadamantane in Low-Temperature Matrices. *Tetrahedron Lett.* **24**, 3887–3890 (1983).
(34) Loss of N_2 from **2b** to generate **3b** could be stimulated both by irradiation with 365 nm light and also by prolonged exposure to synchrotron radiation. In addition to the 50 keV radiation used to acquire the data presented above, we have examined the structure of **2b** as a function of time with both 50 and 37.5 keV radiation without 365 nm irradiation and in both cases observed N_2 loss to generate **3b**·N_2 loss was stimulated. The structure generated by photochemically promoted N_2 loss is identical to that promoted by X-ray stimulated N_2 loss. The X-ray stimulated loss of N_2 is similar to observations made in protein crystallography regarding the cleavage of weak bonds upon extended irradiation as a mechanism to dissipate incipient X-ray energy. See, Garman, E. Radiation damage in macromolecular crystallography: what is it and why should we care? *Acta Cryst. D.* **66**, 339–351 (2010).